3-D Voxel-Based Reconstruction of Multiple Objects Buried in Layered Media by VBIM Hybridized With Unsupervised Machine Learning

Jiawen Li, Yanjin Chen, Jianliang Zhuo, and Feng Han, *Senior Member, IEEE*

***Abstract*— This article presents a novel hybrid electromagnetic inversion method. The traditional 3-D variational Born iterative method (VBIM) is combined with the unsupervised machine-learning expectation maximization (EM). In each iteration, VBIM first outputs the pseudo-randomly distributed model parameters in all discretized cells in the inversion domain. Then the EM algorithm is used to classify them and estimate the mean model parameter values of each homogeneous scatterer or subscatterer supposing that the reconstructed model parameters in all cells comply with the Gaussian mixture model (GMM). At last, partial cells in the inversion domain classified as "background" will be removed and the unknowns in the next VBIM iteration are reduced. This process is implemented iteratively until no "background" cell can be removed anymore and the data misfit between the measured scattered field and reconstructed field reaches the stop criterion. Finally, the mean value of the model parameter estimated by EM is mandatorily assigned for each homogeneous scatterer or subscatterer. Numerical examples show that the proposed hybrid method works efficiently for the reconstruction of isotropic, anisotropic, homogeneous, or inhomogeneous scatterers. It also has a certain antinoise ability.**

***Index Terms*— Electromagnetic full-wave inversion (FWI), expectation maximization (EM), machine learning, variational Born iterative method (VBIM).**

I. Introduction

ELECTROMAGNETIC inversion utilizes field data collected at the receiver array to infer the model parameters of unknown targets located in a specific region. It has wide applications for subsurface nondestructive testing [1], airborne transient electromagnetics [2], geophysical well logging [3], through the wall imaging [4], unexploded ordnance identification [5], etc. In strong electromagnetic scattering applications, i.e., when the contrast of the scatterer with respect to the background medium is high or its electrical size is large, the nonlinearity usually requires iterations to obtain optimized model parameters of scatterers.

There are two types of iterative full-wave inversion (FWI) methods if we classify them according to the availability of *a priori* information of the model parameters in the inversion domain. One is the model-based inversion in which partial *a priori* information is obtained in advance. Consequently, the dimension of the vector of unknowns in the inversion can be immediately reduced or reduced in a transformed domain [6]. This helps to mitigate the ill-posedness of the electromagnetic inverse problem and acquire more accurate solutions. However, the model-based inversion usually requires that we know the general locations or approximate shapes of the scatterers before implementing the iterative inversion. On the contrary, the voxel-based inversion directly solves for all the model parameters in all the discretized cells without incorporating any *a priori* information. Because the straightforward way to describe electromagnetic scattering is using the integral equation, it is convenient to formulate the voxel-based FWI in the framework of the state equation and the data equation [7]. The commonly used methods include the Born iterative method (BIM), contrast source inversion (CSI), and subspace-based optimization method (SOM), etc. In the BIM [8], the state and data equations are solved alternately to update the total fields and model parameters alternately [9]. Different from BIM, CSI has no forward computation [10]. The cost function is constructed using the summation of mismatches in the data equation and the state equation. The induced current and dielectric contrasts in the inversion domain are updated alternately until the total mismatches reach minima [11]. SOM is implemented similar to CSI but for a subspace of the induced current [12], [13]. There are also several variants related to the aforementioned three methods such as distorted BIM (DBIM) or variational BIM (VBIM) [9], [14]. Detailed voxel-based electromagnetic FWI methods are summarized in [15] and readers can refer to it. These methods can be used to reconstruct the dielectric parameters of 3-D scatterers with arbitrary inhomogeneity. However, the iteration computational cost is also high, especially for the scatterer with large electrical size.

Thanks to the fast development of computing technology in recent years, various artificial neural networks (ANN) are being widely used in electromagnetic FWI. Compared with the traditional iterative methods, the FWI based on ANN has the obvious advantage of fast computation in online prediction. It can be categorized into four kinds [16]. The first kind is the direct learning in which the ANN directly learns the mapping relation between the model parameters of the scatterers and the recorded scattered field at the receiver

Manuscript received April 6, 2021; revised May 17, 2021; accepted June 13, 2021. Date of publication June 25, 2021; date of current version January 12, 2022. This work was supported by the National Key Research and Development Program of the Ministry of Science and Technology of China under Grant 2018YFF01013300. *(Corresponding author: Feng Han.)*

The authors are with the Key Laboratory of Electromagnetic Wave Science and Detection Technology, Institute of Electromagnetics and Acoustics, Xiamen University, Xiamen 361005, China (e-mail: feng.han@xmu.edu.cn).

Digital Object Identifier 10.1109/TGRS.2021.3089631

array in the training. The design architecture of ANN in the direct learning is straightforward. However, the ANN must spend unnecessary cost to train and learn the underlying wave physics of electromagnetic scattering. Representative works have been presented in [17]–[19]. The second kind is learning-assisted objective-function approach in which the ANN and the traditional iterative solver are hybridized. The ANN usually provides preliminary dielectric images of scatterers, and traditional FWI iterations are implemented starting from these preliminary images. For example, in [20] and [21], the convolutional neural network (CNN) is first used to reconstruct the dielectric images from magnetic resonance or ultrasound images of tissues, and then the traditional iterative method is used to further refine the dielectric parameter distribution of the tissues. In [22], the Contrast Source Net is proposed to learn the total contrast source, which effectively improves the reconstruction accuracy of the following connected iterative solver. In [23], the CNN U-Net first finds the compressed inversion domain, which is close to the true shape of the scatterer, and then the BIM is implemented to invert for the dielectric parameters of the scatterer in the downsized computational region. Because the FWI starts from good initial values of the model parameters, the final reconstructed parameters are more accurate. The third kind is the physics-assisted learning approach, which is also a kind of hybrid method. However, compared with the second method, the ANN is used to reconstruct the final model parameters of the scatterers instead of the iterative solver. The input of the ANN is usually a preliminary image of the scatterer, which is often obtained by an approximate inverse solver, e.g., Born approximation (BA) or back propagation (BP). Related research work has been presented in [17], [24]–[27]. The advantage of this kind of method is that both the input and output of the ANN have the same data type, usually the scatterer dielectric images. Therefore, we can directly adopt the mature ANN structure used in image processing almost without modification. Besides these three kinds, there are also other ways to combine ANN and electromagnetic inversion. For example, in [28], Wei and Chen proposed the induced current-learning method. They cascaded several CNNs with relatively simple structures and completed the final inversion of dielectric parameters by learning the equivalent current on the scatterer step by step. Summary and review of the ANN and applications to electromagnetic inversion can be referred to in [29], [30]. In addition, there is another type of learning-based electromagnetic FWI, which utilizes the support vector machine (SVM) to localize the underground buried object. Compared with ANN, it can avoid the typical drawbacks such as overfitting or local minima occurrence. Readers can refer to [29], [31] for the application of SVM to FWI.

However, in most of the aforementioned works, machine learning is supervised, i.e., the ANN must be trained by a large number of samples before being used to perform the nonlinear inversion. In this article, we explore the possible hybridization of unsupervised machine learning and traditional 3-D voxel-based iterative inversion. As we know, both the supervised and unsupervised machine-learning techniques heavily depend on sample data. Only when the system learns from enough historical sample data can it build the precise prediction models. The prediction accuracy depends upon the amount of data. In the 3-D voxel-based electromagnetic inversion, there are two sets of sample data, the scattered field data recorded at all the receivers and the model parameters in all the discretized cells in the inversion domain. We will focus on the second set in this work and assume that all the scatterers in the inversion domain can be divided into several homogeneous subscatterers. Because the 3-D voxel-based electromagnetic inversion problem is usually ill-posed and underdetermined, the model parameters in all discretized cells solved by the iterative method, e.g., VBIM, are pseudorandom when the number of discretized cells is large enough [32]. According to the central limit theorem of the statistics, the reconstructed model parameters in each iteration of VBIM in the discretized cells belonging to each homogeneous subscatterer will automatically follow the Gaussian distribution. Its mean value is close to the true model parameter of each homogeneous subscatterer. If there is more than one model parameter, e.g., both the permittivity and conductivity used to simultaneously depict the homogeneous subscatterer, joint Gaussian distribution can be adopted. Usually, besides the background medium, there are always several homogeneous scatterers or subscatterers in the inversion domain. Therefore, a Gaussian mixture model (GMM) is the best choice to describe the reconstructed model parameter distribution for all the discretized cells in the whole inversion domain. One of the efficient unsupervised machine-learning techniques used to classify the sample data complying with a GMM is the expectation maximization (EM) [33]. In this article, we combine VBIM with the EM algorithm to reconstruct 3-D scatterers embedded in a layered medium. In each iteration, the retrieved model parameters from VBIM are classified by the EM algorithm and the size of the computation domain is reduced. When iterations of VBIM terminate, mandatory assignments of the reconstructed parameter values are implemented to guarantee the consistency of model parameters of all the homogeneous scatterers or subscatterers. The details will be discussed in Section II.

The organization of this article is as follows: In Section II, the forward model and the inversion model for traditional electromagnetic inversion are briefly described. Then the machine-learning EM algorithm and its hybridization with VBIM are presented in detail. In Section III, three numerical examples are presented to verify the proposed hybrid method. The first one is for an isotropic scatterer. The second one demonstrates how to determine the EM classification number and tests the antinoise ability. And in the third example, a fully anisotropic and inhomogeneous scatterer is considered. Finally, in Section IV, conclusions are drawn and discussions are presented.

II. Methods

In this section, we briefly describe the forward and inverse scattering formulas with the volume integral equation. In addition, we will discuss the hybridization of the iterative inversion algorithm VBIM with the machine-learning EM algorithm in detail.

A. Forward Model

The forward model is formulated by the state equations, which can be expressed as

$$\begin{aligned}\mathbf{E}^n_{\text{inc}}(\mathbf{r}) &= \mathbf{E}^n_{\text{tot}}(\mathbf{r}) - \mathbf{E}^n_{\text{sct}}(\mathbf{r}) = \overline{\overline{\epsilon}}^{-1}(\mathbf{r})\frac{\mathbf{D}^n_{\text{tot}}(\mathbf{r})}{\varepsilon_0} \\ &\quad - j\omega\int_D \overline{\overline{\mathbf{G}}}^{nm}_{\mathbf{EJ}}(\mathbf{r},\mathbf{r}')\cdot\overline{\overline{\chi}}_\epsilon(\mathbf{r}')\mathbf{D}^m_{\text{tot}}(\mathbf{r}')d\mathbf{r}' \\ &\quad - j\omega\int_D \overline{\overline{\mathbf{G}}}^{nm}_{\mathbf{EM}}(\mathbf{r},\mathbf{r}')\cdot\overline{\overline{\chi}}_\mu(\mathbf{r}')\mathbf{B}^m_{\text{tot}}(\mathbf{r}')d\mathbf{r}' \qquad (1a)\end{aligned}$$

$$\begin{aligned}\mathbf{H}^n_{\text{inc}}(\mathbf{r}) &= \mathbf{H}^n_{\text{tot}}(\mathbf{r}) - \mathbf{H}^n_{\text{sct}}(\mathbf{r}) = \overline{\overline{\mu}}^{-1}(\mathbf{r})\frac{\mathbf{B}^n_{\text{tot}}(\mathbf{r})}{\mu_0} \\ &\quad - j\omega\int_D \overline{\overline{\mathbf{G}}}^{nm}_{\mathbf{HJ}}(\mathbf{r},\mathbf{r}')\cdot\overline{\overline{\chi}}_\epsilon(\mathbf{r}')\mathbf{D}^m_{\text{tot}}(\mathbf{r}')d\mathbf{r}' \\ &\quad - j\omega\int_D \overline{\overline{\mathbf{G}}}^{nm}_{\mathbf{HM}}(\mathbf{r},\mathbf{r}')\cdot\overline{\overline{\chi}}_\mu(\mathbf{r}')\mathbf{B}^m_{\text{tot}}(\mathbf{r}')d\mathbf{r}' \qquad (1b)\end{aligned}$$

where $\mathbf{E}^n_{\text{inc}}$ and $\mathbf{H}^n_{\text{inc}}$ are the incident fields evaluated in the nth layer when the scatterers are absent. $\mathbf{D}^n_{\text{tot}}$ and $\mathbf{B}^n_{\text{tot}}$ are the total flux densities in the nth layer when the scatterers are present. $\overline{\overline{\mathbf{G}}}^{nm}_{\mathbf{EJ}}$, $\overline{\overline{\mathbf{G}}}^{nm}_{\mathbf{EM}}$, $\overline{\overline{\mathbf{G}}}^{nm}_{\mathbf{HJ}}$, and $\overline{\overline{\mathbf{G}}}^{nm}_{\mathbf{HM}}$ are the layered medium dyadic Green's functions [34] linking scatterers in the mth layer and field values in the nth layer. Equation (1) is formulated for the anisotropic magnetodielectric scattering scenario and its weak forms can be found in [35]. However, it is straightforward to simplify it to account for isotropic scattering [36] or nonmagnetic scattering scenarios [37]. In the forward scattering computation, we let $n = m$ and (1) is discretized and total fields $\mathbf{D}^m_{\text{tot}}$ and $\mathbf{B}^m_{\text{tot}}$ are solved by the stabilized biconjugate-gradient fast Fourier transform (BCGS-FFT) [35], [38], [39].

B. Inversion Model

The inversion model is formulated by the data equations, which can be expressed as

$$\begin{aligned}\mathbf{E}^n_{\text{sct}}(\mathbf{r}) &= j\omega\int_D \overline{\overline{\mathbf{G}}}^{nm}_{\mathbf{EJ}}(\mathbf{r},\mathbf{r}')\cdot\overline{\overline{\chi}}_\epsilon(\mathbf{r}')\mathbf{D}^m_{\text{tot}}(\mathbf{r}')d\mathbf{r}' \\ &\quad + j\omega\int_D \overline{\overline{\mathbf{G}}}^{nm}_{\mathbf{EM}}(\mathbf{r},\mathbf{r}')\cdot\overline{\overline{\chi}}_\mu(\mathbf{r}')\mathbf{B}^m_{\text{tot}}(\mathbf{r}')d\mathbf{r}' \qquad (2a)\\ \mathbf{H}^n_{\text{sct}}(\mathbf{r}) &= j\omega\int_D \overline{\overline{\mathbf{G}}}^{nm}_{\mathbf{HJ}}(\mathbf{r},\mathbf{r}')\cdot\overline{\overline{\chi}}_\epsilon(\mathbf{r}')\mathbf{D}^m_{\text{tot}}(\mathbf{r}')d\mathbf{r}' \\ &\quad + j\omega\int_D \overline{\overline{\mathbf{G}}}^{nm}_{\mathbf{HM}}(\mathbf{r},\mathbf{r}')\cdot\overline{\overline{\chi}}_\mu(\mathbf{r}')\mathbf{B}^m_{\text{tot}}(\mathbf{r}')d\mathbf{r}' \qquad (2b)\end{aligned}$$

where $\mathbf{E}^n_{\text{sct}}$ and $\mathbf{H}^n_{\text{sct}}$ are the scattered fields measured at the receiver arrays in the nth layer. In the inverse scattering computation, (2) is discretized and the model parameters $\overline{\overline{\chi}}$ are solved by VBIM [14], [35], [40], [41]. For electromagnetic iterative inversion, (1) and (2) are solved alternately, and thus the total fields and contrasts are updated alternately until the misfit of measured scattered field reaches a stop criterion.

C. EM Algorithms Applied to VBIM Results

As mentioned in Section I, the reconstructed model parameters in all the discretized cells in each VBIM iteration step comply with the GMM model. The machine-learning EM algorithm based on maximum likelihood estimation (MLE) is the proper choice to classify the discretized cells. In the expectation step (E-step), the mean and variance for each Gaussian distribution are fixed, and the datasets are classified. In other words, the Gaussian probability of the model parameters in each cell is calculated according to the known mean and variance. Then we determine to which homogeneous medium each discretized cell is belonging. In the maximum step (M-step), the mean and variance for each Gaussian distribution are recalculated by MLE based on the classification obtained in the last E-step. In other words, we update the mean and variance of each Gaussian distribution according to the new cell classification obtained in the last E-step. This iteration continues until all the model parameters converge. Because the application of the machine-learning EM algorithm to the GMM data is quite mature [42], we will not discuss it in detail here.

Algorithm 1 EM

procedure
  $Initialize\ \omega_i^1,\ \mu_{mi}^1$ and σ_{mi}^1
  //ω_i is the weighting factor.
  //μ_{mi} is the mean of the mth model parameter.
  //σ_{mi} is the variance of the mth model parameter.
classification:
  for each $k \in [1 \ldots K]$ **do**
    //K is the maximum iteration number.
    for each $n \in [1 \ldots N]$ **do** //N is the cell number.
      for each $i \in [0, 1 \ldots I]$ **do**
        //I is homogeneous subscatterer number.
        $P_{in}^k = \prod_{m=1}^{M} \frac{1}{\sqrt{2\pi}\sigma_{mi}^k}\exp\left(-\frac{\left(s_m-\mu_{mi}^k\right)^2}{2\left(\sigma_{mi}^k\right)^2}\right)$
        //P_{in}^k is the probability value.
        //s_m is mth model parameter from VBIM.
      end for
    end for
    for each $n \in [1 \ldots N]$ **do**
      Label(n) = argmax$_i$ P_{in}^k //classification
    end for
    for each $i \in [0, 1 \ldots I]$ **do**
      get ω_i^{k+1}, μ_{mi}^{k+1} and σ_{mi}^{k+1} //MLE
    end for
    if $\sum_{\substack{0\leqslant i\leqslant I\\ 1\leqslant m\leqslant M}} \frac{|\mu_{mi}^{k+1}-\mu_{mi}^k|}{|\mu_{mi}^k|} \leqslant 0.001$ **then**
      goto *end*
    end if
  end for
end:
end procedure

Assume that the whole 3-D inversion domain is discretized into N cells, and there is only one isolated homogeneous scatterer embedded in the inversion domain. Suppose the background medium takes N_0 cells and the scatterer takes N_1 cells. So, $N = N_0 + N_1$. In GMM, the first Gaussian distribution corresponds to the background dielectric parameters. The second one corresponds to the scatterer dielectric parameters. The machine-learning EM algorithm is useful to classify the model parameters in all discretized cells reconstructed by VBIM

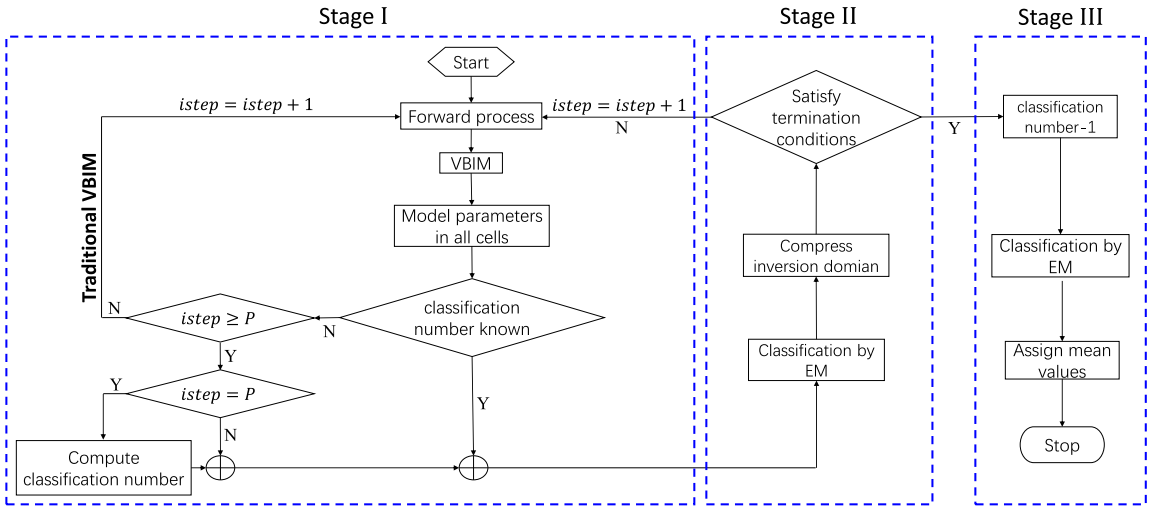

Fig. 1. Flowchart of the VBIM-EM hybridization. In Stage I, the traditional VBIM is implemented to reconstruct the model parameters in all the discretized cells. The EM classification number is also computed in this stage if it is unknown. In Stage II, the EM classification is implemented and partial "background" cells are removed to compress the inversion domain. In Stage III, the mean values are assigned to the model parameters of homogeneous subscatterers. Stages I and II are coupled with each other. When the EM classification in Stage II is complete, we return to Stage I to implement the VBIM again.

and estimate the true dielectric parameters. In addition, it is easy to extend this procedure to account for inhomogeneous scatterers, which can be divided into several homogeneous subscatterers. The detailed procedure of EM classification and parameter estimation for the results from VBIM is given in Algorithm 1. Here, we want to emphasize three points. First, the machine-learning EM algorithm usually depends on the initial solutions. The results from VBIM are used as the initial solutions of EM. Second, if the number of model parameter types is more than one, e.g., when both relative permittivity and conductivity are reconstructed, the joint Gaussian distribution is used. The label given for a certain cell by EM classification is the same for all the model parameter types in that cell. This guarantees the structural consistency. Third, the covariance matrix is not considered in the joint distribution. We assume all model parameters, e.g., relative permittivity and conductivity, are independent of each other in the MLE employed by the EM algorithm.

D. Hybridization of VBIM and EM

As mentioned in Section IV, in each VBIM iteration, the machine learning EM algorithm is used to classify the reconstructed model parameters in all the discretized cells and estimate the mean values of the background medium as well as all the homogeneous subscatterers. Before we substitute these refined model parameters back to the forward model to implement the BCGS-FFT again, partial cells classified as "background" will be removed to compress the inversion domain. Here, the "removed" means the model parameters in these cells will not be assembled into the discretized matrix equation in the next round VBIM iteration because "background" cells have no contribution to the scattered fields at the receiver arrays. It is worth mentioning that the removal of "background" cells is only applied to the inversion VBIM algorithm. For the forward computation by BCGS-FFT, the computational domain keeps unchanged, i.e., the removed "background" cells still remain. The whole process of the hybridization of VBIM and EM can be divided into three stages. The flowchart is shown in Fig. 1.

1) Stage I (Only VBIM and Computation of the Classification Number): The model parameters in all the discretized cells remaining (i.e., not "removed") in the inversion domain are reconstructed by VBIM. If the EM classification number is known, i.e., we know how many homogeneous media are existing in the inversion domain, the program directly shifts to Stage II when VBIM terminates. When the classification number is unknown, the pure VBIM is implemented P times. And then we take the following strategy to compute the classification number. As illustrated in Algorithm 1, there are I homogeneous subscatterers in the inversion domain. We guess a number S, which is much larger than I, and obligatorily perform the EM classification supposing there are S types of homogeneous media (i.e., there are S Gaussian distributions in the GMM). As a result, many mean values of the S Gaussian distributions from MLE will almost overlap. Then we can set a threshold or several thresholds to merge the Gaussian distributions. In other words, if the mean values of two Gaussian distributions are very close, they are treated as the same Gaussian distribution. Following this procedure, the redundant Gaussian distributions in the GMM are gradually removed and the number of the final remaining Gaussian distributions is the true classification number (i.e., the number of the homogeneous media in the inversion domain). This procedure is more clearly shown by the second numerical example in Section III. In addition, one should note that the P times implementation of VBIM is necessary before we merge the Gaussian distributions. The initial solutions of VBIM are the parameters of the background medium. Only when the VBIM is implemented several times can the parameter difference among different homogeneous subscatterers or between the background medium and scatterers show up.

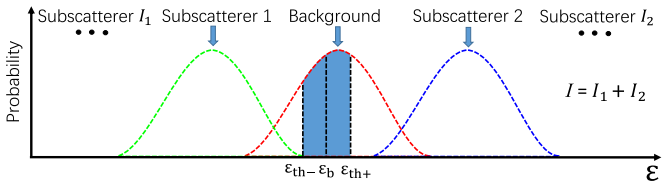

Fig. 2. Scheme to remove the "background" cells corresponding to the shadow regions. ε_{th-} and ε_{th+} are two thresholds corresponding the equality of (3). ε_b is the true relative permittivity of the background medium.

2) Stage II (VBIM-EM and EM Classification): The procedure of EM classification of the reconstructed model parameters in the inversion domain is shown in Algorithm 1. After mean values of all the classes are evaluated by MLE, partial discretized cells classified as "background" will be removed to compress the inversion domain because they have no contribution to the scattered fields. This will gradually lower the computation cost of VBIM. As shown in Fig. 2, we first pick the Gaussian distribution for the background medium, i.e., find these cells classified as "background." However, we cannot directly remove all these cells. The machine-learning EM algorithm is based on the statistical model. Some cells belonging to the scatterers may be incorrectly judged as "background." Therefore, we set a threshold to remove partial "background" cells with their reconstructed model parameter values close to the true model parameter values of the background medium. As shown in Fig. 2, we take the GMM for the relative permittivity as the example. The nth cell satisfying

$$\frac{|\varepsilon_n - \varepsilon_b|}{\max\limits_{1 \leqslant n \leqslant N_b} (|\varepsilon_n - \varepsilon_b|)} \leqslant \text{th} \tag{3}$$

will be removed. When the equality of (3) holds, there are two solutions ε_{th-} and ε_{th+}, which are labeled in Fig. 2. The N_b in (3) is the total number of cells classified as "background" by the EM algorithm, and th is a user-defined variable that is larger than zero but smaller than one. A larger value of th means more "background" cells are removed in each iteration. However, some cells belonging to the scatterer may be incorrectly removed with a higher probability. When th is smaller, fewer "background" cells are removed in each VBIM iteration, and the convergence becomes slower. The ε_b is the true background parameter, which is not necessarily the same as the mean value of the Gaussian distribution for the "background" cells. Once the thresholds ε_{th-} and ε_{th+} are obtained, the cells corresponding to the shadow region shown in Fig. 2 will be removed. When there are multiple model parameters, e.g., relative permittivity and conductivity in the GMM, we can set independent threshold for each parameter but use the same th value. Only a "background" cell with all their model parameters satisfying the similar condition of (3) will be removed.

One should note that Stages I and II are coupled together. After partial "background" cells are removed in Stage II, we need to go back to Stage I to implement the VBIM again, as shown in Fig. 1. The termination condition of the coupled Stages I and II includes two aspects, which must be satisfied simultaneously. The first one is that no "background" cells can be removed anymore. The second one is that the data misfit between the measured scattered field and the computed value by BCGS-FFT-VBIM are smaller than a prescribed value or the data misfit almost keeps unchanged in the iterations.

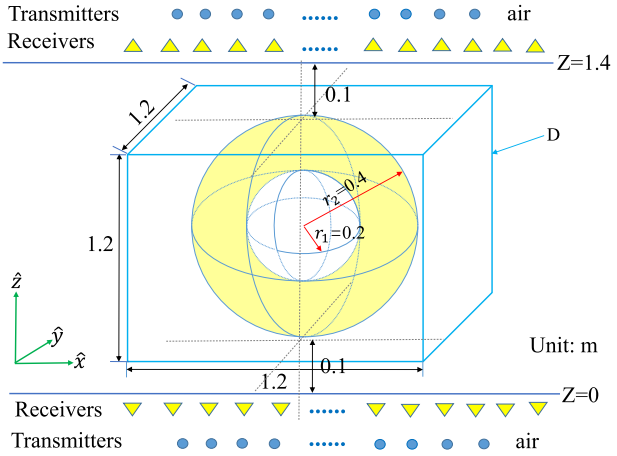

Fig. 3. Configuration of the inversion model with a dual-layer sphere embedded in the middle layer.

3) Stage III (Mean Value Assignments): When Stage II terminates, almost all the "background" cells have been removed. So, we reduce the EM classification number by one and implement the EM classification again based on the new classification number. Finally, we assign the mean values evaluated by MLE for a certain class to the model parameters of the cells belonging to that class. Such an assignment is reasonable for a homogeneous subscatterer in the inversion domain.

E. Comparisons With Pure VBIM

The hybrid VBIM-EM method proposed in this work utilizes the classical machine-learning technique EM to classify the reconstructed model parameters in the inversion domain. Partial discretized cells classified as "background" are gradually removed in successive iterations. Finally, the assignment of mean values for the remaining cells in the inversion domain is performed. The proposed hybrid method outperforms the pure VBIM in two aspects. One is the improved reconstruction accuracy. This is because the machine-learning EM algorithm helps to gradually compress the inversion domain and reduce the number of unknowns in the discretized data equation. However, the scattered field data remain unchanged in the whole process. Consequently, the ill-posedness of the inverse problem is actually mitigated. The VBIM becomes easier to find the optimized solution. The other one is the lowered computation cost of VBIM-EM. Because the inversion domain is compressed, both the time and memory consumption of VBIM-EM is lower than those of the pure VBIM. These two aspects are shown in the first numerical example in Section III.

F. Comparisons With Other Hybrid Methods

In the proposed hybrid VBIM-EM, the "background" cells are gradually removed in successive iterations. The iterative

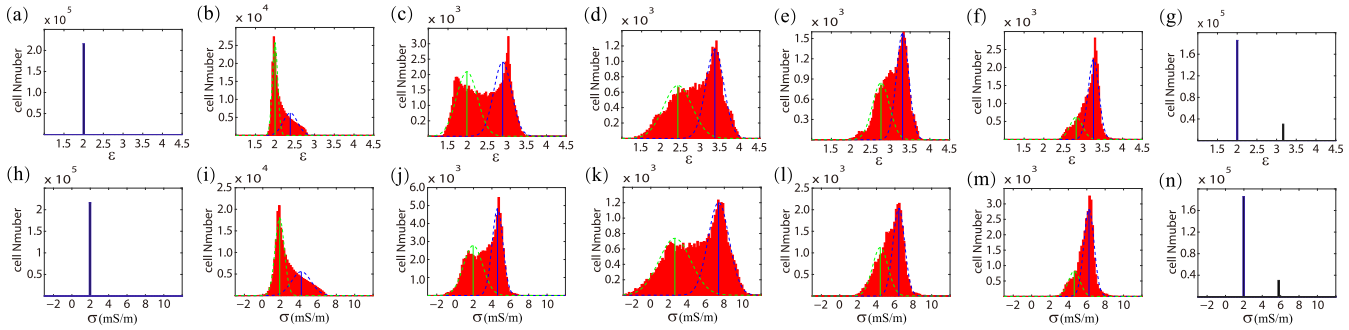

Fig. 4. Histograms of the reconstructed model parameters in different iteration steps. From left to right, they are in 1st, 2nd, 4th, 7th, 11th, 17th, and 18th step. The first 17 steps belong to the coupled Stages I and II. The last 18th step belongs to Stage III. (a)–(g) are for relative permittivity. (h)–(n) are for conductivity. The dotted curves are GMM curves used to fit the histograms.

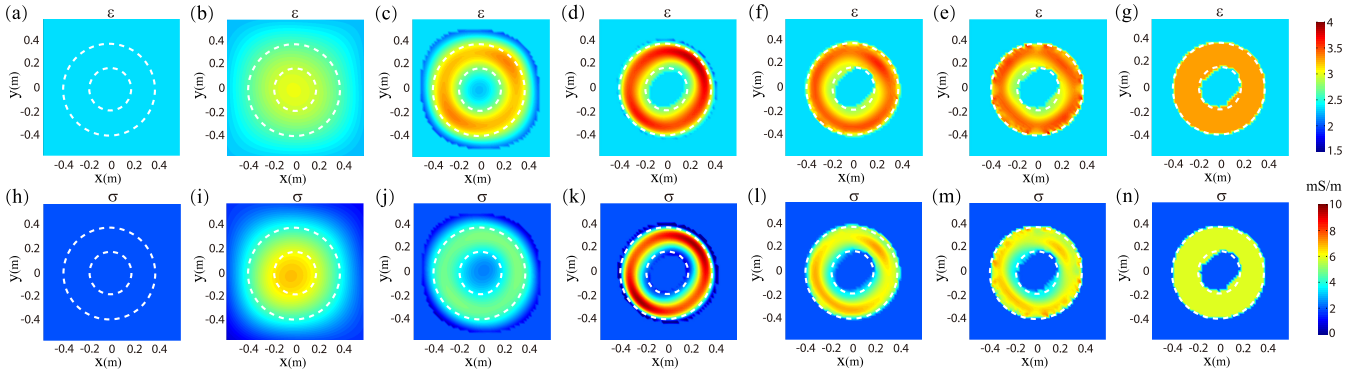

Fig. 5. Reconstructed 2-D slices at $z = 0.7$ m corresponding to the iteration steps given in Fig. 4. Dotted circles denote the true scatterer.

multiscaling approach (IMSA) proposed in [43] and [44] improves the inversion resolution by means of the similar method. However, VBIM-EM and IMSA are different in several aspects. In VBIM-EM, the FWI loop, i.e., VBIM is only implemented once. In IMSA, it is actually the inner loop of two nested loops and thus implemented several times. In IMSA, the grid discretization is dynamically adjusted. When the whole process approaches the end, the resolution can be very high. However, in VBIM-EM, the grid discretization is fixed. When the whole process approaches the end, the resolution remains unchanged, although the inversion domain becomes smaller. In each outer loop of IMSA, the inversion domain is compressed. In the full-wave iterations, the inversion domain keeps the same. However, in VBIM-EM, the inversion domain is compressed as the full-wave iterations (i.e., VBIM) continue. In addition, one should note that the proposed hybrid VBIM-EM is also different from the previous work [45], [46] in which only the "background" cells and the "scatterer" cells are distinguished. However, in this work, different subscatterers are also distinguished and the model parameters of each kind of medium are also estimated by MLE.

III. Numerical Results

In this section, we use three numerical examples to verify the VBIM-EM algorithm. The background medium includes three layers. The top and bottom layers are air. The scatterers are embedded in the middle layer. The transmitter and receiver arrays are placed in the top and bottom layers. In the first case, the scatterer is isotropic and homogeneous. The classification number is known. It is used to demonstrate the feasibility of VBIM-EM and show its advantage over the pure VBIM. In the second case, there are three homogeneous scatterers embedded in the middle layer. Two scatterers have the same model parameters. We will show how to determine the classification number for EM and test the antinoise ability of VBIM-EM in this case. In the third case, the scatterer is arbitrary anisotropic and inhomogeneous. It will be divided into several homogeneous subscatterers by the EM algorithm. All the measured scattered field data are simulated by the BCGS-FFT solver. The th in (3) is set as 20% for all three cases and this value is also verified as an appropriate value by all three cases. All the inversions are performed on a workstation with 20-cores Xeon E2650 v3 2.3 G CPU, 512 GB RAM.

A. Dual-Layer Sphere Embedded in the Middle Layer

As shown in Fig. 3, the inner radius of the sphere is $r_1 = 0.2$ m and its outer radius is $r_2 = 0.4$ m. Its center is located at (0, 0, 0.7) m. The dielectric parameters of the inner sphere and the background are the same. They are $\varepsilon = 2.0$ and $\sigma = 2$ mS/m. The outer sphere has dielectric parameters $\varepsilon = 3.2$ and $\sigma = 6$ mS/m. The inversion domain D enclosing the object has the dimensions of 1.2 m × 1.2 m × 1.2 m. Its center is also located at (0, 0, 0.7) m and is divided into

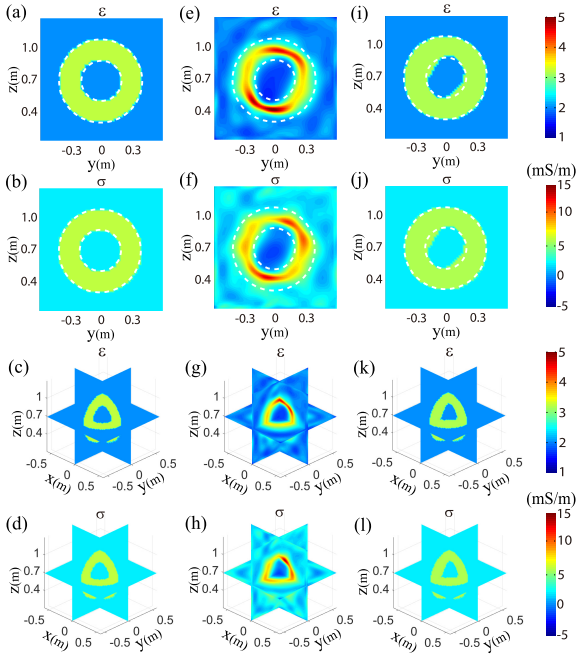

Fig. 6. Ground truth and the 2-D and 3-D inversion results by VBIM and VBIM-EM. (a)–(d) are the 2-D and 3-D ground truth profiles. (e)–(h) are the 2-D and 3-D profiles reconstructed by VBIM. (i)–(l) are the 2-D and 3-D profiles reconstructed by VBIM-EM.

$60 \times 60 \times 60$ cells. The size of each cell is $\Delta x = \Delta y = \Delta z = 0.02$ m. So, there are totally 432 thousand unknowns to be reconstructed. The 98 transmitters are uniformly located in two 4.2 m $\times$ 4.2 m planes at $z = -0.2$ m and $z = 1.6$ m, respectively. The operating frequency is 150 MHz. The scattered fields are collected by 128 receiver arrays uniformly located in two 5.6 m $\times$ 5.6 m planes at $z = -0.1$ m and $z = 1.5$ m, respectively. Thus, there are 150 528 data equations if we detach the real and imaginary parts of the scattered fields.

In each iteration step, we use the GMM including two Gaussian distributions to fit the reconstructed model parameters from VBIM. Fig. 4 shows the histograms of reconstructed model parameters fitted by GMM curves in the 1st, 2nd, 4th, 7th, 11th, 17th, and 18th steps. The first 17 steps belong to the coupled Stages I and II. The last 18th step belongs to Stage III. Fig. 5 shows the xy plane 2-D slices of the VBIM results in these steps. At the beginning, the model parameters in all discretized cells in the whole inversion domain are assigned as the background parameters, as shown in Fig. 5(a) and (h). The histogram in Fig. 4 shows a straight line. In following steps, the "background" cells are gradually removed by VBIM-EM and the peak value of the Gaussian distribution curve for the "background" medium decreases synchronously. In the 2nd step, the "background" cells are much more than the "scatterer" cells. Only one Gaussian distribution peak obviously shows up in the histogram. Correspondingly, in Fig. 5(b) and (i), the scatterer only has an embryo. However, in the 4th step, a lot of "background" cells have been removed. Two peaks obviously show up in the histograms. The general shape of the sphere can be seen in Fig. 5(c) and (j). As the VBIM-EM iterations going on,

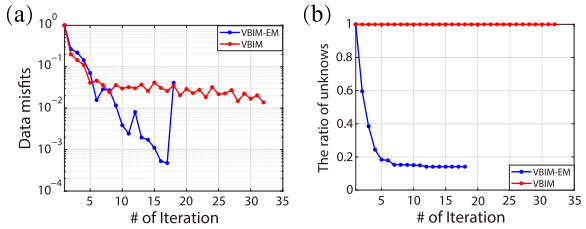

Fig. 7. Converging processes of VBIM with and without the EM algorithm. (a) Variations of data misfits of the scattered fields in different iteration steps. (b) Ratio of unknowns in different iteration steps to the total unknowns in the first step.

more and more "background" cells are removed. And in the 17th step, most "background" cells have been removed. The pattern of the sphere is clearly shown in Fig. 5(e) and (m). In the last 18th step (belonging to Stage III), the model parameters of the scatterer are mandatorily assigned as the mean values from VBIM-EM, leading to the clear shapes shown in Fig. 5(g) and (n).

Fig. 6 shows the comparisons of ground truth and the final reconstructed model parameters by VBIM with and without the machine-learning EM algorithm. The dotted circles in the 2-D slices denote the true location of the dual-layer sphere. Clearly, the VBIM-EM outperforms VBIM. Not only the retrieved values of model parameters are more precise when the machine-learning EM algorithm is applied but also a better shape match is provided by VBIM-EM.

To quantitatively compare the performance of VBIM-EM and VBIM, we use the data misfit and model misfit defined in (8) of [35]. The data misfit indicates how well the measured scattered field at the receiver arrays matches the computed value from BCGS-FFT-VBIM. The model misfit indicates how well the reconstructed model parameters in the inversion domain match their true profiles. Fig. 7(a) shows the variations of data misfits of the scattered fields in each iteration step. Several observations are made. 1) VBIM-EM converges faster than VBIM. But it is not as stable as VBIM because of the interference of EM. 2) Before the last step, the data misfits in VBIM-EM are obviously smaller than those in VBIM. 3) In the last step, the data misfit of VBIM-EM suddenly increases. The reconstructed shape of the sphere does not exactly occupy the true location. Thus, the mandatory assignments of mean values in Stage III of VBIM-EM change the model parameters in some cells greatly, leading to the sudden increase of the data misfit. Fig. 7(b) shows the variations of the remaining cells in the computation domain in each iteration step. As can been seen, the number of unknowns decreases quickly in the first five steps for VBIM-EM. After this, it changes slowly. This is because after the 5th step most "background" cells have been removed and only a small number of cells are removed in the following steps. By contrast, in VBIM, the cell number keeps unchanged in all iterations. This also confirms the low data misfits of VBIM-EM before the last step shown in Fig. 7(a). Because the computation domain is compressed by the EM algorithm, the number of unknowns is decreased. As a result, the uncertainty of the solutions of VBIM is mitigated. When the iterations terminate, the model misfits of permittivity and conductivity of the reconstructed results by VBIM are 11.4%

TABLE I

VARIATIONS OF WEIGHTS AND MEAN VALUES OF ε AND σ FOR ALL THE EM CLASSES IN DIFFERENT ITERATIVE EM CLASSIFICATION STEPS

Ite#	CN	Noise free (weight (%), mean of ε, mean of σ (mS/m))				20 dB noise (weight (%), mean of ε, mean of σ (mS/m))			
1	9	(0.02,1.50,-0.9) (21.8,2.07,2.37)	(4.15,1.83,1.14) (8.57,2.26,3.19)	(10.7,1.89,1.47) (5.29,2.50,4.32)	(41.4,1.98,1.90) (5.30,2.77,5.63) (2.83,3.37,8.74)	(0.02,1.43,-1.2) (73.6,1.98,1.95)	(0.05,1.49,-0.8) (11.5,2.26,3.28)	(0.49,2.35,0.33) (4.96,2.54,4.54)	(2.14,1.72,0.49) (4.45,2.80,5.78) (2.85,3.39,8.91)
2	8	(0.06,1.51,-0.5) (15.3,2.14,2.68)	(4.66,1.82,1.06) (7.53,2.40,3.87)	(12.9,1.90,1.53) (6.60,2.73,5.46)	(50.1,2.00,1.99) (2.83,3.38,8.74)	(0.02,1.43,-1.2) (10.9,2.27,3.30)	(0.04,1.49,-0.8) (4.82,2.54,4.55)	(2.00,1.72,0.42) (4.32,2.79,5.75)	(74.7,1.99,1.95) (3.23,3.31,8.28)
3	7	(4.25,1.81,1.02)	(12.6,1.90,1.51) (7.90,2.38,3.80)	(50.1,1.99,1.98) (6.79,2.73,5.43)	(15.6,2.13,2.64) (2.83,3.38,8.74)	(0.07,1.48,-0.9)	(0.43,2.34,0.15) (12.6,2.31,3.53)	(2.05,1.72,0.45) (6.95,2.72,5.44)	(75.1,1.99,1.96) (2.83,3.41,8.93)
4	6	(4.05,1.80,0.98)	(12.5,1.90,1.52)	(54.7,2.00,2.01) (10.8,2.63,4.95)	(15.1,2.19,2.92) (2.85,3.38,8.73)	(0.06,1.47,-1.0)	(1.97,1.72,0.38)	(75.8,1.99,1.96) (6.75,2.72,5.43)	(12.3,2.32,3.54) (3.06,3.36,8.55)
5	5	(5.53,1.80,1.07)	(66.8,1.99,1.94)	(14.2,2.20,2.95)	(10.6,2.63,4.97) (2.85,3.38,8.72)	(5.52,1.94,-0.6)	(1.58,1.71,0.55)	(78.5,2.00,1.99)	(16.4,2.50,4.40) (3.00,3.39,8.80)
6	4	(5.41,1.80,1.07)	(67.7,1.99,1.95)	(14.3,2.22,3.04)	(12.6,2.81,5.87)	(0.94,1.72,0.31)	(77.1,1.99,1.97)	(13.5,2.38,3.83)	(8.51,3.02,6.84)
7	3		(72.9,1.98,1.92)	(11.9,2.22,3.03)	(15.2,2.68,5.21)		(80.6,1.99,1.96)	(12.7,2.42,4.02)	(6.72,3.05,7.00)

Remark: Ite# denotes the iteration #; CN denotes the classification number.

TABLE II

BACKGROUND PARAMETERS OF THE MIDDLE LAYER AND THE TRUE AND RECONSTRUCTED MODEL PARAMETERS OF SCATTERERS

Parameter / object	ε_{11}	ε_{12}	ε_{13}	ε_{22}	ε_{23}	ε_{33}	μ_{11}	μ_{12}	μ_{13}	μ_{22}	μ_{23}	μ_{33}	σ_{11}	σ_{12}	σ_{13}	σ_{22}	σ_{23}	σ_{33}
Middle layer	1.5	0.0	0.0	1.5	0.0	2.0	1.2	0.0	0.0	1.2	0.0	1.8	1.0	0.0	0.0	1.0	0.0	2.0
Outer cube (true)	2.0	0.5	0.3	1.8	0.3	2.5	1.5	0.2	0.5	1.8	0.2	2.2	2.0	2.0	3.0	5.0	1.0	4.0
Outer cube (reconstructed)	2.01	0.46	0.31	1.80	0.30	2.53	1.51	0.21	0.46	1.75	0.21	2.22	2.15	2.06	2.95	4.62	1.09	4.18
Inner cube (true)	2.4	0.2	0.6	2.0	0.5	3.2	1.8	0.5	0.2	1.4	0.4	2.7	5.0	4.0	4.0	2.0	3.0	8.0
Inner cube (reconstructed)	2.31	0.27	0.53	1.96	0.45	3.04	1.74	0.43	0.27	1.49	0.35	2.61	4.40	3.55	3.76	2.71	2.54	7.01

Remark: the unit of σ is mS/m.

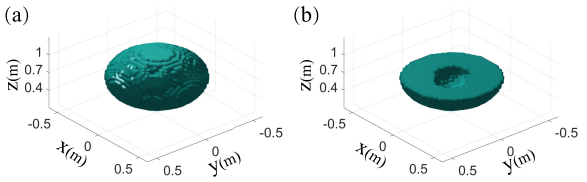

Fig. 8. Iso-surfaces of the final reconstructed structure. (a) Whole sphere. (b) Dissected half sphere.

and 38.6%, respectively. However, they are 5.3% and 13.4% when VBIM-EM is adopted. In each iteration step, the VBIM takes 101 min and consumes 249 GB memory. By contrast, the VBIM-EM only needs 15 min and 38 GB memory in the last iteration step although they are the same as those of VBIM at the beginning. Obviously, VBIM-EM outperforms VBIM for both the reconstruction accuracy and computation cost. Fig. 8 shows the iso-surfaces of the structure of the reconstructed dual-layer sphere. Because the inner sphere has the same dielectric parameters as those of the background medium, the sphere appears hollow.

B. Three Objects Embedded in the Middle Layer

As shown in Fig. 9, there are three homogeneous objects embedded in the inversion domain. The dimensions of the cuboid are 0.32 m × 0.32 m × 0.64 m. The cube has the dimensions of 0.32 m × 0.32 m × 0.32 m. The radius of the sphere is 0.28 m. The dielectric parameters of the second layer are the same as those in the last case. The cuboid and the cube have the same model parameters $\varepsilon = 3.6$ and $\sigma = 10$ mS/m. The relative permittivity and conductivity of

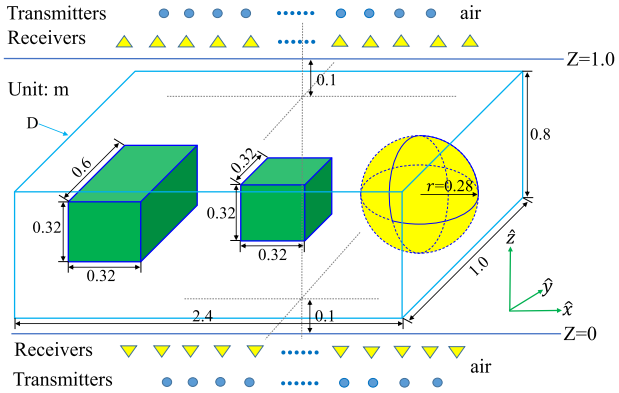

Fig. 9. Configuration of the inversion model with three objects embedded in the middle layer. The cuboid and cube have the same model parameters.

the sphere are 2.8 and 6 mS/m, respectively. The inversion domain D enclosing the three objects has the dimensions of 2.4 m × 1.0 m × 0.8 m. Its center is located at (0, 0, 0.5) m and is divided into 120 × 50 × 40 cells. The size of each cell is $\Delta x = \Delta y = \Delta z = 0.02$ m. The 100 transmitters are uniformly located in two 5.4 m × 2.4 m planes at $z = -0.2$ m and $z = 1.2$ m, respectively. The operating frequency is also 150 MHz. The scattered fields are collected by 144 receivers arrays uniformly located in two 6.6 m × 3.0 m planes at $z = -0.1$ m and $z = 1.1$ m, respectively.

Because the cuboid and cube have the same dielectric parameters, there are totally three kinds of homogeneous media in the inversion domain. If this a priori information is unknown, we first implement the pure VBIM four times (i.e., $P = 4$ in the flowchart of Fig. 1). The inversion results are

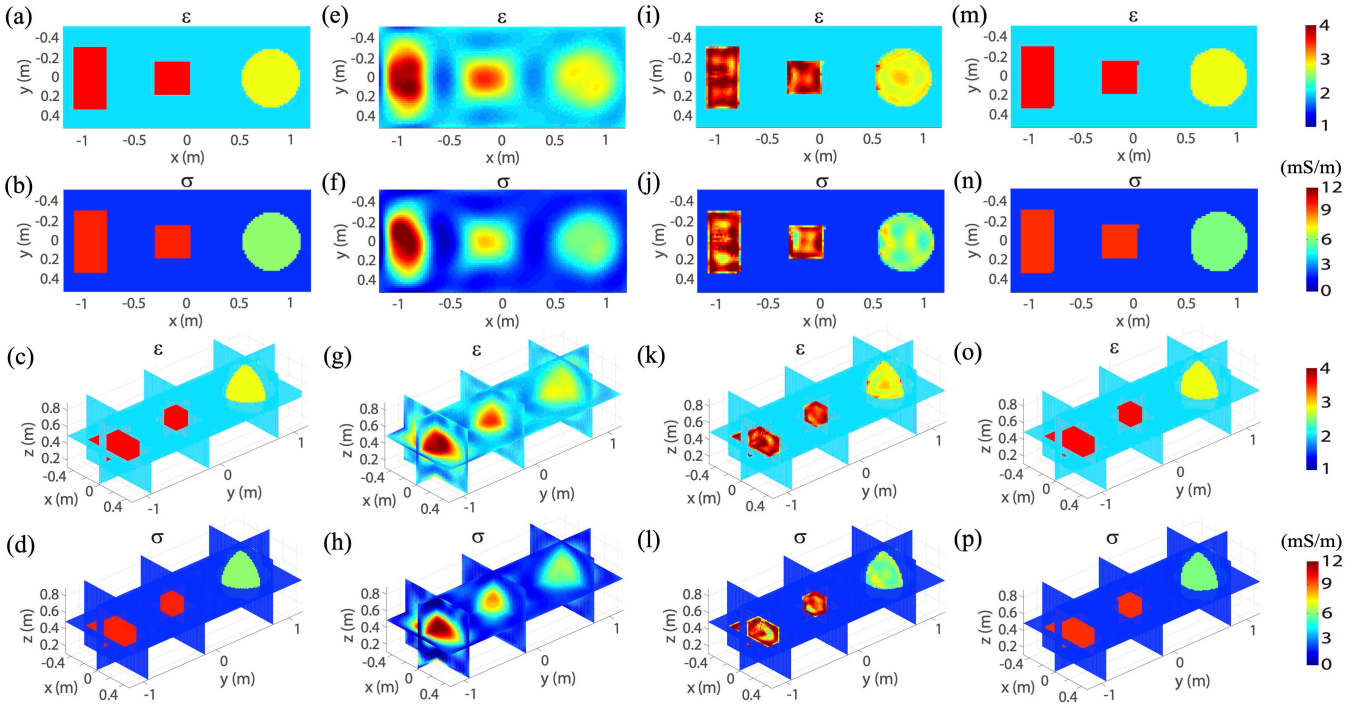

Fig. 10. Ground truth and the 2-D and 3-D inversion results by VBIM and VBIM-EM. (a)–(d) are the 2-D and 3-D ground truth profiles. (e)–(h) are the 2-D and 3-D profiles reconstructed by VBIM in the 4th step, which will be used to compute the classification number. (i)–(l) are the 2-D and 3-D profiles reconstructed by VBIM-EM in the last step of coupled Stages I and II. (m)–(p) are the 2-D and 3-D profiles obtained by the assignments of mean values in Stage III.

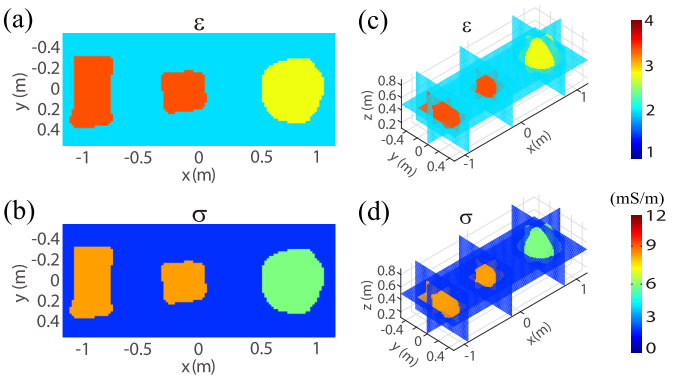

Fig. 11. Inversion results of the three objects by VBIM-EM when 20 dB noise is added. (a) and (b) are 2-D profiles. (c) and (d) are 3-D profiles.

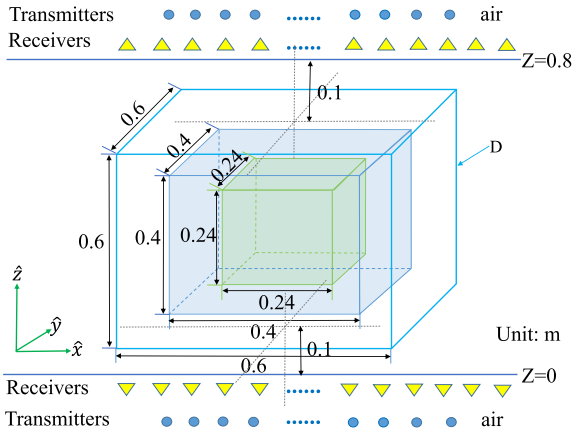

Fig. 12. Configuration of the inversion model with nested cubes embedded in the middle layer. The inner cube dimensions are 0.24 m × 0.24 m × 0.24 m and the outer cube dimensions are 0.4 m × 0.4 m × 0.4 m.

shown in Fig. 10(e)–(h). We can see the difference between the scatterers and the background medium is obvious enough to estimate the classification number. We then guess there are totally nine types of homogeneous media in the inversion domain, which are much more than the true homogeneous medium types. Then, based on the reconstructed model parameters in the fourth step, we perform the EM classification iteratively. The results in each step are listed in Table I. In each iteration step, we reduce the classification number by one if the estimated parameters by MLE satisfy one of the following conditions: 1) the weight of a certain class is less than 1% and 2) the difference of the mean values for relative permittivity between two classes is less than 0.3 and the difference for conductivity is less than 1 mS/m. The weight in (1) is the ratio of discretized cells belonging to a certain class with respect to the total cells in the inversion domain. And its selection is empirical. For example, if the number of total cells classified by EM as a certain class is less than 2400 and because the number of total cells in the inversion domain is 240 000 in this case, the weight is less than 1% for that class and thus this class will be removed. When both (1) and (2) are not satisfied, the iterative EM classification procedure summarized in Table I terminates. The number of remaining classes is the true classification number. One interesting observation is that there is one class that has an obvious larger weight than the weights of all other classes in all the iteration steps for both noise-free and noisy cases. Definitely, this class is the background medium.

When 20 dB noise is added, the above-mentioned iterative procedure can also compute the correct classification number,

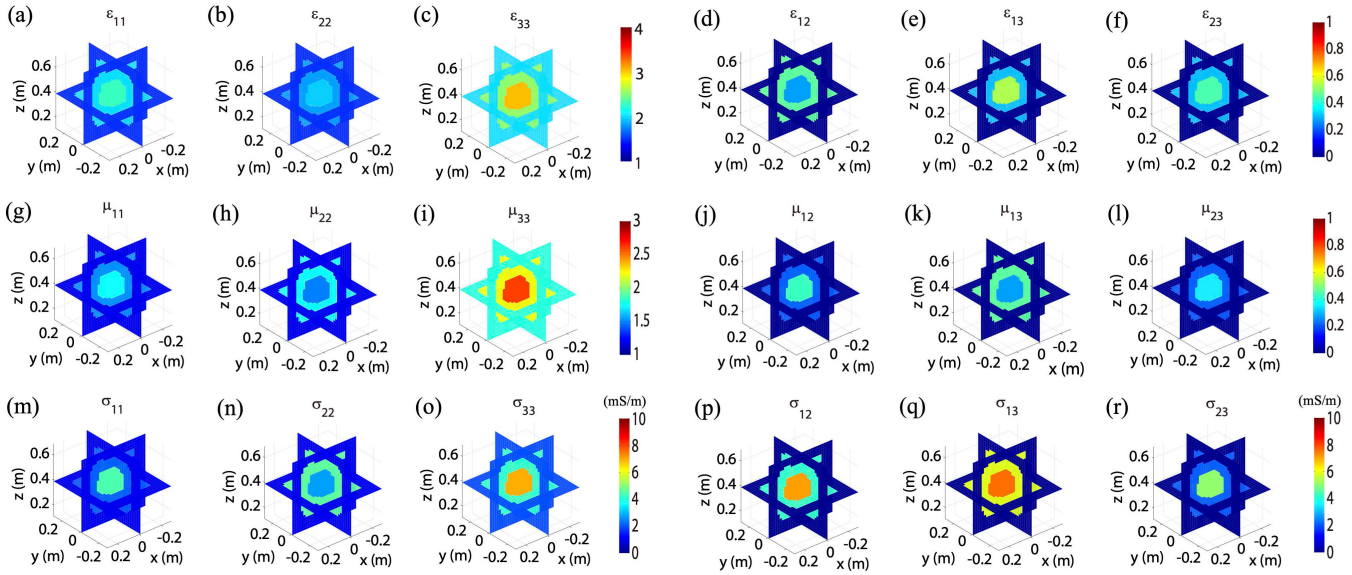

Fig. 13. Final reconstructed 3-D profiles of the nested cubic objects by VBIM-EM. (a)–(f) are for the relative permittivity. (g)–(l) are for the relative permeability. (m)–(r) are for conductivity.

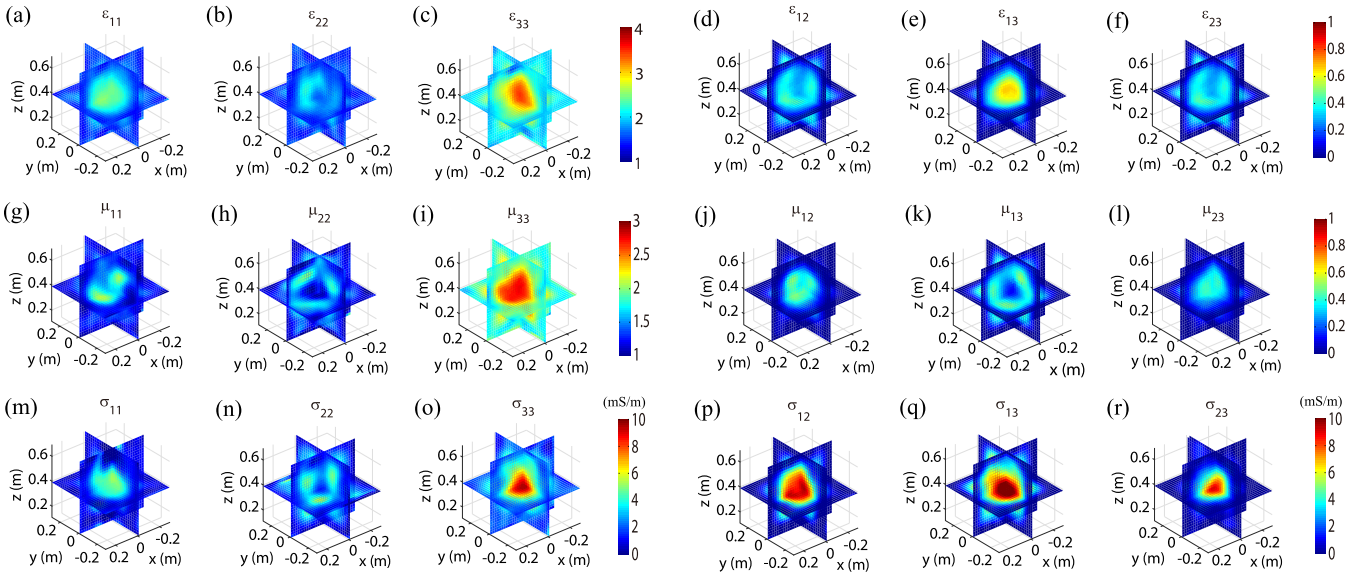

Fig. 14. Final reconstructed 3-D profiles of the nested cubic objects by pure VBIM. (a)–(f) are for the relative permittivity. (g)–(l) are for the relative permeability. (m)–(r) are for conductivity.

as summarized in Table I. By comparing the reconstructed 2-D and 3-D profiles in Figs. 10(m)–(p) and 11, we can see that the noise interference distorts the reconstructed shapes of the homogeneous scatterers. Specifically speaking, some discretized cells in the periphery of a scatterer are not correctly classified by the EM algorithm when noise is added. This incorrect judgment further interferes with the final assigned mean values, which is clearly shown in Fig. 11. The mean values of the reconstructed relative permittivity for the cuboid as well as cube and the sphere are 3.58 and 2.79 when noise free. They are 3.36 and 2.78 when 20 dB noise is added. The mean values of the reconstructed conductivity for the cuboid as well as cube and the sphere are 9.87 and 5.93 mS/m when noise free. They are 8.59 and 5.88 mS/m when 20 dB noise is added. We can see that both the reconstructed shapes and model parameters are still reliable even with noise contamination.

C. Nested Cubes Embedded in the Middle Layer

In this case, we apply the VBIM-EM algorithm to the reconstruction of nested cubes with arbitrary anisotropic parameters embedded in the uniaxial middle layer. As shown in Fig. 12, the nested cubes include the inner and outer layers. The dimensions of the inner cube are 0.24 m × 0.24 m × 0.24 m, and those of the outer cube are 0.4 m × 0.4 m × 0.4 m. The true dielectric parameters of the middle layer, the inner cube, and the outer cube are listed in Table II. The dielectric tensors are assumed symmetrical.

The inversion domain enclosing the objects has the dimensions of 0.6 m × 0.6 m × 0.6 m, and its center is located

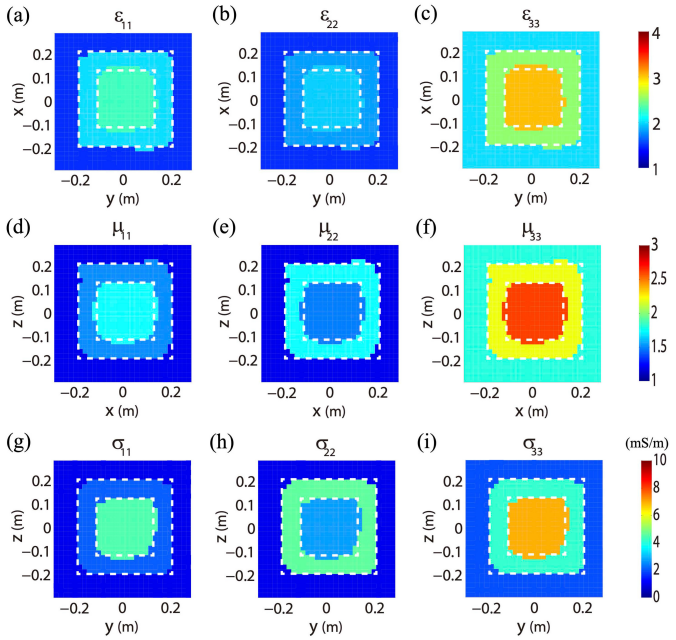

Fig. 15. Final reconstructed 2-D profiles of the nested cubic objects by VBIM-EM. (a)–(c) are the slices at $z = 0.4$ m for the diagonal relative permittivity. (d)–(f) are the slices at $z = 0$ m for the diagonal relative permeability. (g)–(i) are the slices at $z = 0$ m for the diagonal conductivity. Dotted boxes denote the outer and inner cube boundaries.

at (0, 0, 0.4) m. It is divided into 27 000 cells. The size of each cell is $\Delta x = \Delta y = \Delta z = 0.02$ m. So, there are totally 486 000 unknowns to be reconstructed. The 72 transmitters are uniformly placed in two 1.0 m $\times$ 1.0 m planes at $z = -0.2$ m and $z = 1.0$ m, respectively. Two operation frequencies 130 and 160 MHz are chosen. The scattered fields are collected by two arrays of 98 receivers, which are uniformly located at $z = -0.1$ m and $z = 0.9$ m planes, respectively. Thus, there are totally 169 344 data equations.

Fig. 13 shows the inverted 3-D profiles of the nested cubic objects by VBIM-EM, whereas Fig. 14 shows reconstructed profiles by pure VBIM. We can see that the pure VBIM can only find the approximate location of the inhomogeneous scatterer. The boundary between the outer cube and the inner cube is not discernible. Fortunately, this defect is effectively remedied by the proposed hybrid VBIM-EM. Both the shapes and dielectric parameters are well reconstructed. They are more vividly displayed by the 2-D slices in Fig. 15. Although the reconstructed cross sections of both the inner and outer cubes are not exact squares, the general shapes match the squares. However, as the machine-learning EM is a statistical method, the boundaries of the cubes cannot be precisely located, and notches show up near the boundaries.

IV. Conclusion and Discussions

In this article, the traditional FWI method VBIM is hybridized with the machine-learning technique EM. In each VBIM-EM iteration, the VBIM updates the model parameters of the discretized cells in the inversion domain. Then the EM algorithm is used to classify these cells and estimate the mean model parameters for the background medium and the homogeneous subscatterers. In the following, partial "background" cells are removed. This iteration process continues until no "background" cell can be removed anymore and the data misfit between the measured scattered field and the reconstructed field reaches the stop criterion. When the number of homogeneous media in the inversion domain is unknown, we can implement the pure VBIM for a limited number of iterations. Then an iterative EM classification procedure is adopted to compute the true homogeneous medium number before we carry out the hybridized VBIM-EM iterations. Numerical examples show such an iterative EM classification procedure is reliable even when the scattered field data are contaminated by 20 dB noise.

Both the isotropic and anisotropic inverse scattering scenarios are used to verify the proposed hybrid method. Comparisons of the reconstruction of isotropic model parameters show that VBIM-EM outperforms VBIM for not only the higher reconstruction accuracy but also the lower computation cost. When multiple homogeneous scatterers have the same model parameters, the proposed iterative EM classification method in the second numerical example can identify them and correctly treat them as the same class of medium.

We assume each scatterer is homogeneous and an inhomogeneous scatterer can be divided into several homogeneous subscatterers. Such an assumption is reasonable in many practical applications such as microwave imaging of breast cancer [47] and noninvasive inspection of crystals [48]. In an extreme situation in which the scatterer has the continuously varying medium, the assumption of the GMM is not reasonable for model parameters. This issue will be addressed in our future work by using other machining-learning techniques or adding some gradient constraints to the unknown model parameters in the cost function.

References

[1] H. Liu and M. Sato, "*In situ* measurement of pavement thickness and dielectric permittivity by GPR using an antenna array," *NDT E Int.*, vol. 64, pp. 65–71, Jun. 2014.

[2] C. Qiu *et al.*, "Multifrequency 3-D inversion of GREATEM data by BCGS-FFT-BIM," *IEEE Trans. Geosci. Remote Sens.*, vol. 57, no. 4, pp. 2439–2448, Apr. 2019.

[3] H. Wang, "Simultaneous reconstruction of geometric parameter and resistivity around borehole in horizontally stratified formation from multiarray induction logging data," *IEEE Trans. Geosci. Remote Sens.*, vol. 41, no. 1, pp. 81–89, Jan. 2003.

[4] L.-P. Song, C. Yu, and Q. Huo Liu, "Through-wall imaging (TWI) by radar: 2-D tomographic results and analyses," *IEEE Trans. Geosci. Remote Sens.*, vol. 43, no. 12, pp. 2793–2798, Dec. 2005.

[5] L.-P. Song, L. R. Pasion, S. D. Billings, and D. W. Oldenburg, "Nonlinear inversion for multiple objects in transient electromagnetic induction sensing of unexploded ordnance: Technique and applications," *IEEE Trans. Geosci. Remote Sens.*, vol. 49, no. 10, pp. 4007–4020, Oct. 2011.

[6] M. Li, A. Abubakar, and T. M. Habashy, "A three-dimensional model-based inversion algorithm using radial basis functions for microwave data," *IEEE Trans. Antennas Propag.*, vol. 60, no. 7, pp. 3361–3372, Jul. 2012.

[7] Z. Q. Zhang and Q. H. Liu, "Three-dimensional nonlinear image reconstruction for microwave biomedical imaging," *IEEE Trans. Biomed. Eng.*, vol. 51, no. 3, pp. 544–548, Mar. 2004.

[8] Y. M. Wang and W. C. Chew, "An iterative solution of the two-dimensional electromagnetic inverse scattering problem," *Int. J. Imag. Syst. Technol.*, vol. 1, no. 1, pp. 100–108, 1989.

[9] F. Li, Q. H. Liu, and L.-P. Song, "Three-dimensional reconstruction of objects buried in layered media using born and distorted born iterative methods," *IEEE Geosci. Remote Sens. Lett.*, vol. 1, no. 2, pp. 107–111, Apr. 2004.

[10] P. M. V. D. Berg and R. E. Kleinman, "A contrast source inversion method," *Inverse Problems*, vol. 13, no. 6, pp. 1607–1620, Dec. 1997.

[11] P. M. V. D. Berg, A. L. V. Broekhoven, and A. Abubakar, "Extended contrast source inversion," *Inverse Problems*, vol. 15, no. 5, pp. 1325–1344, Oct. 1999.

[12] X. Chen, "Application of signal-subspace and optimization methods in reconstructing extended scatterers," *J. Opt. Soc. Amer. A, Opt. Image Sci.*, vol. 26, no. 4, pp. 1022–1026, Mar. 2009.

[13] X. Chen, "Subspace-based optimization method for solving inverse-scattering problems," *IEEE Trans. Geosci. Remote Sens.*, vol. 48, no. 1, pp. 42–49, Jan. 2010.

[14] N. Zaiping, Y. Feng, Z. Yanwen, and Z. Yerong, "Variational born iteration method and its applications to hybrid inversion," *IEEE Trans. Geosci. Remote Sens.*, vol. 38, no. 4, pp. 1709–1715, Jul. 2000.

[15] X. Chen, Ed., *Computational Methods for Electromagnetic Inverse Scattering*. Singapore: Wiley, 2018.

[16] X. Chen, Z. Wei, M. Li, and P. Rocca, "A review of deep learning approaches for inverse scattering problems (invited review)," *Prog. Electromagn. Res.*, vol. 167, pp. 67–81, Mar. 2020.

[17] Z. Wei and X. Chen, "Deep-learning schemes for full-wave nonlinear inverse scattering problems," *IEEE Trans. Geosci. Remote Sens.*, vol. 57, no. 4, pp. 1849–1860, Apr. 2019.

[18] H. M. Yao, W. E. I. Sha, and L. Jiang, "Two-step enhanced deep learning approach for electromagnetic inverse scattering problems," *IEEE Antennas Wireless Propag. Lett.*, vol. 18, no. 11, pp. 2254–2258, Nov. 2019.

[19] L. Xiao, J. Li, F. Han, W. Shao, and Q. H. Liu, "Dual-module NMM-IEM machine learning for fast electromagnetic inversion of inhomogeneous scatterers with high contrasts and large electrical dimensions," *IEEE Trans. Antennas Propag.*, vol. 68, no. 8, pp. 6245–6255, Aug. 2020.

[20] G. Chen, P. Shah, J. Stang, and M. Moghaddam, "Learning-assisted multimodality dielectric imaging," *IEEE Trans. Antennas Propag.*, vol. 68, no. 3, pp. 2356–2369, Mar. 2020.

[21] P. Mojabi, V. Khoshdel, and J. Lovetri, "Tissue-type classification with uncertainty quantification of microwave and ultrasound breast imaging: A deep learning approach," *IEEE Access*, vol. 8, pp. 182092–182104, Sep. 2020.

[22] Y. Sanghvi, Y. Kalepu, and U. K. Khankhoje, "Embedding deep learning in inverse scattering problems," *IEEE Trans. Comput. Imag.*, vol. 6, pp. 46–56, 2020.

[23] Y. Chen, L.-Y. Xiao, J. Zhuo, F. Han, and Q. H. Liu, "Quantitative electromagnetic inversion of irregular scatterers based on a three-fold hybrid method," *IEEE Trans. Antennas Propag.*, early access, Jun. 2, 2021, doi: 10.1109/TAP.2021.3083775.

[24] L. Li, L. G. Wang, F. L. Teixeira, C. Liu, A. Nehorai, and T. J. Cui, "DeepNIS: Deep neural network for nonlinear electromagnetic inverse scattering," *IEEE Trans. Antennas Propag.*, vol. 67, no. 3, pp. 1819–1828, Mar. 2019.

[25] J. Xiao, J. Li, Y. Chen, F. Han, and Q. H. Liu, "Fast electromagnetic inversion of inhomogeneous scatterers embedded in layered media by born approximation and 3-D U-Net," *IEEE Geosci. Remote Sens. Lett.*, vol. 17, no. 10, pp. 1677–1681, Oct. 2020.

[26] L. Zhang, K. Xu, R. Song, X. Ye, G. Wang, and X. Chen, "Learning-based quantitative microwave imaging with a hybrid input scheme," *IEEE Sensors J.*, vol. 20, no. 24, pp. 15007–15013, Dec. 2020.

[27] Y. Huang, R. Song, K. Xu, X. Ye, C. Li, and X. Chen, "Deep learning-based inverse scattering with structural similarity loss functions," *IEEE Sensors J.*, vol. 21, no. 4, pp. 4900–4907, Feb. 2021.

[28] Z. Wei and X. Chen, "Physics-inspired convolutional neural network for solving full-wave inverse scattering problems," *IEEE Trans. Antennas Propag.*, vol. 67, no. 9, pp. 6138–6148, Sep. 2019.

[29] A. Massa, G. Oliveri, M. Salucci, N. Anselmi, and P. Rocca, "Learning-by-examples techniques as applied to electromagnetics," *J. Electromagn. Waves Appl.*, vol. 32, no. 4, pp. 516–541, Mar. 2018.

[30] A. Massa, D. Marcantonio, X. Chen, M. Li, and M. Salucci, "DNNs as applied to electromagnetics, antennas, and propagation—A review," *IEEE Antennas Wireless Propag. Lett.*, vol. 18, no. 11, pp. 2225–2229, Nov. 2019.

[31] E. Bermani, A. Boni, S. Caorsi, and A. Massa, "An innovative real-time technique for buried object detection," *IEEE Trans. Geosci. Remote Sens.*, vol. 41, no. 4, pp. 927–931, Apr. 2003.

[32] A. Tarantola, Ed., *Inverse Problem Theory and Methods for Model Parameter Estimation*. Philadelphia, PA, USA: Society for Industrial and Applied Mathematics, 2005.

[33] J. Yang *et al.*, "Compressive sensing by learning a Gaussian mixture model from measurements," *IEEE Trans. Image Process.*, vol. 24, no. 1, pp. 106–119, Jan. 2015.

[34] K. A. Michalski and J. R. Mosig, "Multilayered media Green's functions in integral equation formulations," *IEEE Trans. Antennas Propag.*, vol. 45, no. 3, pp. 508–519, Mar. 1997.

[35] J. Li, J. Zhuo, Z. Guan, F. Han, and Q. H. Liu, "3-D electromagnetic scattering and inverse scattering by magnetodielectric objects with arbitrary anisotropy in layered uniaxial media," *IEEE Trans. Antennas Propag.*, vol. 68, no. 2, pp. 1009–1022, Feb. 2020.

[36] W. Zhang and Q. Huo Liu, "Three-dimensional scattering and inverse scattering from objects with simultaneous permittivity and permeability contrasts," *IEEE Trans. Geosci. Remote Sens.*, vol. 53, no. 1, pp. 429–439, Jan. 2015.

[37] K. Yang and A. E. Yilmaz, "FFT-accelerated analysis of scattering from complex dielectrics embedded in uniaxial layered media," *IEEE Geosci. Remote Sens. Lett.*, vol. 10, no. 4, pp. 662–666, Jul. 2013.

[38] Z. Qing Zhang and Q. Huo Liu, "Applications of the BCGS-FFT method to 3-D induction well logging problems," *IEEE Trans. Geosci. Remote Sens.*, vol. 41, no. 5, pp. 998–1004, May 2003.

[39] F. Han, J. Zhuo, N. Liu, Y. Liu, H. Liu, and Q. H. Liu, "Fast solution of electromagnetic scattering for 3-D inhomogeneous anisotropic objects embedded in layered uniaxial media by the BCGS-FFT method," *IEEE Trans. Antennas Propag.*, vol. 67, no. 3, pp. 1748–1759, Mar. 2019.

[40] Y. Chen, P. Wen, F. Han, N. Liu, H. Liu, and Q. H. Liu, "Three-dimensional reconstruction of objects embedded in spherically layered media using variational born iterative method," *IEEE Geosci. Remote Sens. Lett.*, vol. 14, no. 7, pp. 1037–1041, Jul. 2017.

[41] Z. Yu, J. Zhou, Y. Fang, Y. Hu, and Q. H. Liu, "Through-casing hydraulic fracture evaluation by induction logging II: The inversion algorithm and experimental validations," *IEEE Trans. Geosci. Remote Sens.*, vol. 55, no. 2, pp. 1189–1198, Feb. 2017.

[42] J. A. Bilmes, "A gentle tutorial EM algorithm and its application to parameter estimation for Gaussian mixture and hidden Markov models," Univ. Berkeley, Boulder, CO, USA, Tech. Rep. TR-97-021, 1998.

[43] S. Caorsi, M. Donelli, and A. Massa, "Detection, location, and imaging of multiple scatterers by means of the iterative multiscaling method," *IEEE Trans. Microw. Theory Techn.*, vol. 52, no. 4, pp. 1217–1228, Apr. 2004.

[44] D. Franceschini, M. Donelli, R. Azaro, and A. Massa, "Dealing with multifrequency scattering data through the IMSA," *IEEE Trans. Antennas Propag.*, vol. 55, no. 8, pp. 2412–2417, Aug. 2007.

[45] J. Zhuo, L. Ye, F. Han, L. Xiong, and Q. H. Liu, "Multiparametric electromagnetic inversion of 3-D biaxial anisotropic objects embedded in layered uniaxial media using VBIM enhanced by structural consistency constraint," *IEEE Trans. Antennas Propag.*, vol. 68, no. 6, pp. 4774–4785, Jun. 2020.

[46] X. Huang, J. Li, Y. Chen, F. Han, and Q. H. Liu, "Hybrid electromagnetic inversion of 3-D irregular scatterers embedded in layered media by VBIM and MET," *IEEE Trans. Antennas Propag.*, vol. 68, no. 12, pp. 8238–8243, Dec. 2020.

[47] M. Klemm, J. A. Leendertz, D. Gibbins, I. J. Craddock, A. Preece, and R. Benjamin, "Microwave radar-based differential breast cancer imaging: Imaging in homogeneous breast phantoms and low contrast scenarios," *IEEE Trans. Antennas Propag.*, vol. 58, no. 7, pp. 2337–2344, Jul. 2010.

[48] P. P. Natali, L. Montalto, D. Rinaldi, F. Davi, N. Paone, and L. Scalise, "Noninvasive inspection of anisotropic crystals: Innovative photoelasticity-based methods," *IEEE Trans. Nucl. Sci.*, vol. 65, no. 8, pp. 2203–2207, Aug. 2018.